

# Constraining the Origins of Radio Emission in Radio-quiet QSOs with High-Resolution Observations from the Very Large Array

TREVOR MCCAFFREY<sup>1,2</sup> AND AMY E KIMBALL<sup>2</sup>

<sup>1</sup>*Drexel University Department of Physics, 32 S. 32nd Street, Philadelphia, PA 19104, USA*

<sup>2</sup>*National Radio Astronomy Observatory, 1003 Lopezville Rd, Socorro, NM 87801, USA*

## ABSTRACT

We present high resolution ( $\sim 0.33''$ ) observations taken with the Very Large Array (VLA) of the 124 radio-quiet ( $L_{6\text{GHz}} < 10^{23}\text{W Hz}^{-1}$ ) QSOs (RQQs) from the homogeneous, optically selected, volume-limited ( $0.2 < z < 0.3$ ) sample of 178 QSOs introduced by Kimball et al. (2011). While Kellermann et al. (2016) showed that all of these RQQs were unresolved in their previous  $3.5''$  observations ( $\sim 14\text{kpc}$  at  $z = 0.25$ ), we resolve notable complex structures in at least 41% of the RQQs studied herein. The median flux density of our observations is lower than that measured in Kellermann et al. (2016) by  $\approx 15\%$ , which we interpret as being due to the presence of diffuse extended emission, possibly originating from star formation activity, effectively being filtered out by the longer baselines of our observations. We also utilize the cadence of our two observing periods, as well as image cutouts (where available) from FIRST (Becker et al. 1995) and preliminary “Quick Look” images from Epoch 1 of the VLA Sky Survey (VLASS; Lacy et al. 2020), to construct light curves over decadal timescales of a selected subset of 29 of our radio-quiet sources, as well as the cores of 27 -intermediate and 14 -loud sources selected from Kimball et al. (2011) and Kellermann et al. (2016). As the observing frequencies of FIRST (1.4 GHz) and VLASS (3 GHz) do not match our C-band observations, we must assume a spectral index  $\alpha$  to allow us to intercompare their flux densities with ours. We find that while the light curves are essentially indistinguishable between the three classes of QSOs, the radio-quiet sources must have steep spectral indices ( $\alpha \approx -0.7$ ) and the radio-louds require flat spectral indices ( $\alpha \approx 0.0$ ) to produce physically realistic light curves. Such results indicate that the underlying physics occurring within the inner-kiloparsec region of the two populations of QSOs must ultimately be different.

## 1. INTRODUCTION

Since the discovery of the first quasi-stellar objects (QSOs; Schmidt 1963), our knowledge regarding their radio emission has long been at a stalemate. While it is known that in the radio-loud (RL) population, emission is powered predominantly by jets from their active galactic nuclei (AGN) because of, among other lines of reasoning, structures extending distances far beyond the QSO host galaxy, and extremely high brightness temperatures that must originate from nonthermal processes ( $> 40,000\text{K}$ ), the source of radio emission in their radio-quiet (RQ) counterparts is still very much a matter of debate within the AGN community. Groups have argued that star formation processes are the most likely contributor (Kimball et al. 2011; Condon et al. 2013; Kellermann et al. 2016), while others have argued from both a theoretical (Giustini & Proga 2019) and empirical (Zakamska & Greene 2014; Zakamska et al. 2016) standpoint that star formation simply is not powerful enough and radiation-line-driven winds are more plausible.

A large problem that blurs the question of “what is the dominant source of radio emission in RQQs?” is that most images of RQQs are very ambiguous. Indeed, Kellermann et al. (2016) showed that virtually all RQQs

are unresolved on galaxy scales ( $\sim 14\text{kpc}$  at  $z \sim 0.25$ ). While this showed that the nature of radio emission in RQ sources is clearly very different from that of the RL objects, it presents the idea of RQQs as being a monolithic class of objects—which they are not. Higher resolution observations are needed to distinguish the myriad natures of RQQs.

Another problem that arises when addressing the demographics of RQQs is a lack of proper representation of the RQ population in sample selection. Many approaches to the problem addressed herein rely on radio-selected samples—which are inherently biased towards the RL population—or do not satisfy the optical criterion of being a true QSO ( $M_B < -23$ ), so low luminosity AGN (LLAGN) are included. Even when careful steps in sample selection are taken, in many cases, most RQQs are simply too faint to probe their entire population in typical investigations of color-selected QSO samples, so only upper limits for radio luminosities are attainable. Kimball et al. (2011) address all of the aforementioned shortcomings—presenting an optically selected, volume-limited ( $0.2 < z < 0.3$ ), and volume-complete sample of 178 QSOs that hence truly represents the full diversity

of the wide range of physical properties observed in the Sloan Digital Sky Survey (SDSS; Abazajian et al. 2009).

As the sample described in Kimball et al. (2011) represents a fiducial study of the low-redshift QSO population, it also provides an ideal laboratory for further probing the radio demographics of low-redshift RQQs. In this write-up, results of follow-up VLA A-configuration ( $\sim 0.33''$ ) observations of the RQ subset of sources from Kimball et al. (2011) and Kellermann et al. (2016) are presented, which were previously all unresolved in C-configuration ( $\sim 3.5''$ ).

We aim to resolve emission structures of RQQs within the host galaxies of AGN to reveal further information concerning the morphologies present throughout the RQ population. We do this with the goal in mind of utilizing the VLA as a spatial filter: switching array configurations to longer baselines should “resolve out” diffuse extended emission, if present. We find that at least 41% of RQQs have complex morphologies on  $\gtrsim 1.3\text{kpc}$  scales. We also find that our measured median sample flux density decreases  $\sim 15\%$  from observations by Kellermann et al. (2016) in C-configuration. While variability does play a significant role in shaping our results, we cannot attribute this change as being entirely due to variability as we’d expect changes in both the positive and negative directions to be equally likely (Hovatta et al. 2007).

Given the cadence of these two observing campaigns ( $\sim 8$  years apart) and complementary synoptic radio sky surveys (FIRST observations from 1993–2003; Epoch 1 of VLASS 2017–2019), we are also given a unique opportunity to study the variability of RQQs over decadal timescales. We consider a subset of 29 of our RQQs where useful FIRST data is attainable to cross compare light curves with the cores of 27 radio-intermediate QSOs (RIQs) and 14 RLQs from the complete Kimball et al. (2011) sample. Similarities in the variable behavior between the three classes of QSOs would indicate similar physics occurring in the cores of each of those classes (Barvainis et al. 2005).

As this variability analysis takes advantage of imaging results at different observing frequencies (FIRST at 1.4 GHz; VLASS at 3 GHz) than what we consider here, we must adopt a spectral index to shift these measurements to our preferred 6 GHz. We show that while the RQ and RL sources are indistinguishable in terms of the appearances of their light curves, construction of physically meaningful light curves demands that RQQs are dominated by steep spectrum synchrotron emission ( $\alpha \approx -0.7$ ), and the RLQs dominated by flat spectrum ( $\alpha \approx 0.0$ ) emission from an optically opaque core. Future work unifying radio observations and changes in optical spectroscopy would dictate whether the observed radio variability in RQQs is correlated with changes in high-ionization optical emission lines, which would indicate that the physical origins of radio emission in QSOs must be related to the optical origin(s) (e.g., due to en-

hancements of accretion activity Kunert-Bajraszewska et al. 2020).

In Section 2, we discuss our sample selection for this paper. Section 3 describes our observation and data reduction techniques. Section 4 presents our results in their current state (the end of the Summer 2020 NRAO REU program), and we summarize our findings in Section 5.

A flat  $\Lambda$ CDM cosmology, with  $H_0 = 70 \text{ km s}^{-1}\text{Mpc}^{-1}$ ,  $\Omega_\Lambda = 0.7$ , and  $\Omega_M = 0.3$ , is assumed in calculations throughout this paper (where calculations are performed using the cosmology calculator constructed by Wright 2006).

## 2. TARGETS

Our sample consists of the 124 RQQs studied in the optically selected, volume-complete sample of 178 QSOs introduced by Kimball et al. (2011). Radio-“quiet” in the context of Kimball et al. (2011) requires each QSO to have a 6 GHz spectral luminosity  $L_{6\text{GHz}} < 10^{23} \text{ W Hz}^{-1}$ . While selection of our parent sample is described in further detail in that paper, we review their methodology as an important part of why our results are directly applicable to the RQQ population is careful sample selection.

Targets are drawn from the seventh data release of the Sloan Digital Sky Survey quasar catalog (SDSS-DR7; Schneider et al. 2010). Sample selection is guided with the goal in mind of collecting a statistically meaningful sample representing an entire population of QSOs which is bereft of evolutionary effects. As such, the following cuts are made to SDSS-DR7 to obtain the parent sample of QSOs studied in Kimball et al. (2011) and Kellermann et al. (2016):

- The presence of at least one broad emission line with  $\text{FWHM} > 1000 \text{ km/s}$  to validate the presence of an AGN (Richards et al. 2002).
- Exclude FIRST sources selected for follow-up spectroscopy. Our sample is thus purely selected on the basis of optical colors and is not biased towards any radio properties.
- An absolute magnitude cutoff  $M_B < -23$  so as to include only true bona fide QSOs, avoiding possible LLAGN (Schmidt & Green 1983).
- A volume-limited sample  $0.2 < z < 0.3$ . While we cannot ignore the fact that some evolution will inevitably occur over this narrow redshift range, effects are minimal with regards to our science goal in mind. The relatively low redshift range also allows for detections of QSOs with radio luminosities on par with that of medium starburst galaxies ( $L_{6\text{GHz}} \sim 10^{22.5} \text{ W Hz}^{-1}$ ; Condon et al. 2013).

This produces a sample of all 178 true QSOs—both RL and RQ—within a fixed comoving volume. The final

cut we make, which is the only one specific to this paper, is we restrict our targets to be those with 6 GHz spectral luminosities  $L_{6\text{GHz}} < 10^{23}\text{W Hz}^{-1}$ , focusing our analysis on only those QSOs that are firmly radio-quiet. Even possible radio-intermediate ( $10^{23}\text{W Hz}^{-1} < L_{6\text{GHz}} < 10^{24}\text{W Hz}^{-1}$ ) QSOs should not leak into our sample.

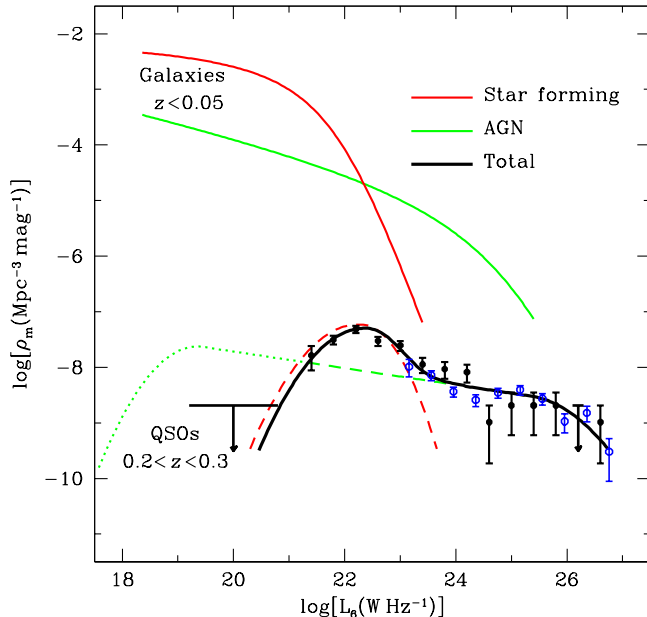


**Figure 1.** Total radio luminosity function (RLF) of low-redshift ( $0.2 < z < 0.3$ ) QSOs (Kimball et al. 2011). Solid black data points indicate the EVLA data obtained in Kimball et al. (2011); open blue data points further constrain the bright end of the RLF and are from an analysis of the radio flux density measurements in NVSS at the SDSS optical position of all  $0.2 < z < 0.45$  QSOs (Condon et al. 2013). The two solid curves in the upper half of the figure represent the nearby ( $z < 0.05$ ) RLFs of galaxies whose radio emission is primarily powered either by star formation (red) or by AGN activity (green). The total 6 GHz RLF (solid black curve) can be well described by two independent components: a parabolic star formation contribution at lower luminosities (dashed red curve), and a flat AGN contribution throughout the entire population (dashed green curve).

The rationale behind this cutoff spectral luminosity function representing a turnover in the radio luminosity function (RLF) and thus the dividing line in QSO populations is described in detail by Kimball et al. (2011), but summarized here. Figure 1 shows the total 6 GHz RLF of quasars within the volume described. Blue data points represent the space density of radio components from positions in the NRAO VLA Sky Survey (NVSS; Condon et al. 1998) coinciding with the optical positions of all QSOs in a lightly extended redshift range,  $0.2 < z < 0.45$ . All of these sources are so strong, they must be powered by AGN. Assum-

ing that the entire QSO population’s radio emission is AGN-dominated and there is no significant difference in how AGN-dominated QSOs behave compared to nearby AGN-dominated galaxies (solid green curve) past a certain characteristic luminosity, extrapolating the NVSS data to lower luminosities produces the dashed green curve—a continuous flat distribution extending to very low-power radio emission. However, utilizing the advent of new high-sensitivity radio telescopes, specifically the NSF’s Karl G. Jansky Very Large Array (VLA), Kimball et al. (2011) showed that the RLF behaves in a markedly different way than the power law distribution that would be expected from extrapolating the NVSS distribution to lower luminosities. In fact, there is a significant bump in the RLF, peaking at  $\sim 10^{22.2}\text{W Hz}^{-1}$  and beginning its turnover at  $\sim 10^{23.3}\text{W Hz}^{-1}$ . This point of turnover occurs just at the same point as the bright end of the RLF of nearby star-forming galaxies, so they proposed that the bump in the RLF of QSOs is due to significant starburst emission present in RQQ host galaxies. Considering all sources below this luminosity cutoff thereby allows us to study the entire RQ population while considering the possibility of star formation processes being the added contributor to the radio emission in RQQs.

### 3. OBSERVATIONS AND DATA REDUCTION

Observations presented in this paper relate to two different, but connected, observing campaigns. The first is that carried out in Kimball et al. (2011) and Kellermann et al. (2016), where VLA C-configuration observations were undergone from October 2010 through January 2011. The other, which we present in detail for the very first time, used the higher-resolution A-configuration and was carried out from August to September of 2019.

#### 3.1. Observations

All A-configuration observations were in the C-band to match the previous 2010/11 results; we note however, that the VLA’s “2019 C-band” covers 4–8GHz whereas its “2011 C-band” was limited to 5–7GHz while the new EVLA was still under commission. Assuming up to 15% loss of usable bandwidth due to known RFI effects in this frequency range, we expect to retain approximately 3.4 GHz of useful bandwidth in image construction and other data reduction techniques.

The 2010/11 observations yielded a typical angular resolution of  $\sim 3.5''$  (corresponding to  $\sim 14\text{kpc}$  at  $z = 0.25$ ) at a 6 GHz reference frequency. Using this knowledge, the previous observations were designed so that emission structures within the QSO host galaxy would remain unresolved, thus mitigating any strictly resolution-based effects in the previous investigation of target flux density measurements (i.e. no flux is “resolved out”). Switching to the VLA’s A-configuration in this paper improves our angular resolution significantly ( $\sim 0.33''$  or  $\sim 1.3\text{kpc}$  at  $z = 0.25$ ), allowing us to dive into the QSO host galaxy and potentially re-

veal complex intermediate subgalactic structure extending distances between the outskirts of a galaxy, and the compact AGN emission that would require very long baseline interferometry (VLBI) observing techniques to view (e.g., Ulvestad et al. 2005). One element of these follow-up observations that must be considered is that we can no longer ignore resolution effects regarding flux density measurements. However, this is not a limitation; rather, results indicating radio emission being “resolved out” will not leave a gap in our knowledge—it will reveal crucial information about the very nature of the radio emission from any given QSO.

For our follow-up A-configuration observations, we calculated necessary exposure times using the VLA Exposure Calculator Tool<sup>1</sup>. We based exposure times on being able to reach a  $5\text{-}\sigma_{\text{rms}}$  detection based on the flux density measurements from Kellermann et al. (2016). The seven faintest sources ( $S_{6\text{GHz}} < 27\mu\text{Jy}$ ) required on-source exposure times ranging from 20–40 minutes. For the next six faintest sources ( $27\mu\text{Jy} < S_{6\text{GHz}} < 33.5\mu\text{Jy}$ ), we aimed to reach a sensitivity of  $\sim 5.5\mu\text{Jy bm}^{-1}$ , requiring 15 minutes of on-source exposure time. The rest of the targets were bright enough to obtain sufficient signal-to-noise in just 10-minute VLA snapshots, reaching a sensitivity of  $\sim 6.68\mu\text{Jy}$ . Observations for these targets were split into two separate 5-minute scans at two different hour angles to obtain better  $uv$ -coverage.

We used quasar 3C 286 as our flux density calibrator and employed standard phase referencing techniques throughout every observation.

### 3.2. Data Reduction

The Common Astronomy Software Application package 5.6.2–3 (CASA; McMullin et al. 2007) was used to reduce our VLA data and perform all imaging in this analysis. After raw data was obtained, the standard VLA pipeline was run to automatically flag and calibrate bad data. While we inspected needs for further flagging in each science target observation, we found that the pipeline largely handled any potentially harmful data points in our raw data effectively, and we could proceed with our imaging analysis most often directly after one successful pipeline run.

While the imaging process is largely tunable and several small details may differ from target to target, we outline our general process for imaging here. The task `tclean` was used with the “natural” weighting scheme for all images. We used a pixel size of  $0.06''$  in order to adequately sample the typical width of our synthesized beam ( $\sim 0.33''$ ). Based on the quality of an initial dirty image created, we chose a meaningful stopping peak residual threshold (typically  $\sim 21\mu\text{Jy}$  for the 10-minute snapshots) to clean down to and imaged the full

primary beam ( $\sim 7.3' \times 7.3'$ ) as a first attempt at including any potential bright sources that could contaminate the area around our central target if left outside the field of view.

From this point on, there were generally three routes we could take in imaging: (i) the image had been sufficiently cleaned and we moved on; (ii) the cleaning process diverged, but the field was sparse so the stopping threshold should be increased; (iii) the cleaning process diverged, and the field was contaminated by other bright sources or exhibited obvious residual phase errors so an iterative phase self-calibration process should be introduced before re-running `tclean`. If this standard procedure is insufficient in reaching our expected noise levels, we typically have to introduce non-standard imaging algorithms built in to CASA. For example, we employ multi-frequency synthesis to account for the wide bandwidth of all targets, but it by default only uses one term in a Taylor expansion to model the C-band spectrum as flat. Using a multi-term multi-frequency synthesis (MT-MFS; Rau & Cornwell 2011) with `nterms=2` more accurately models the spectra of bright sources within the field and thus generally improves the noise levels in our final image. For images severely affected by contaminating sources along the primary beam even after several iterations of self-calibration, we introduce a more computationally-expensive gridding, `aw-project` (Cornwell et al. 2005; Jagannathan et al. 2018), as an attempt to account for both severe wide-bandwidth and wide-field defects.

Distributions of total 6 GHz spectral flux densities and luminosities, as well as the ratio  $R$  between radio and optical  $i$ -band flux densities, are shown in Figure 2. Complete results regarding the radio and optical properties of the 124 RQQs discussed herein are given in Tables 1 and 2 of the Appendix, respectively.

## 4. ANALYSIS

We now have an unbiased homogeneous sample of QSOs that is prudent to undergo a comprehensive study of the low-redshift RQQ population. The most pressing question addressing said population is related to their dominant origin(s) of radio emission. Key issues to investigate herein thus should relate specifically to how results between the two periods of observing compare, and what physical origins could explain such results.

### 4.1. Morphologies

It is known that all RQQs in our restricted redshift range are unresolved on typical host galaxy scales ( $\sim 14\text{kpc}$ ; Kellermann et al. 2016). Moreover, this is perhaps the primary factor that separates RQQs from their counterpart RLQs, of which many can have powerful, collimated radio jets or lobes extending distances far beyond their host galaxy. If RQQs possess features that are resolved on scales between the VLA’s A- and C-configuration, we will then reveal telling information

<sup>1</sup> <https://obs.vla.nrao.edu/ect/>

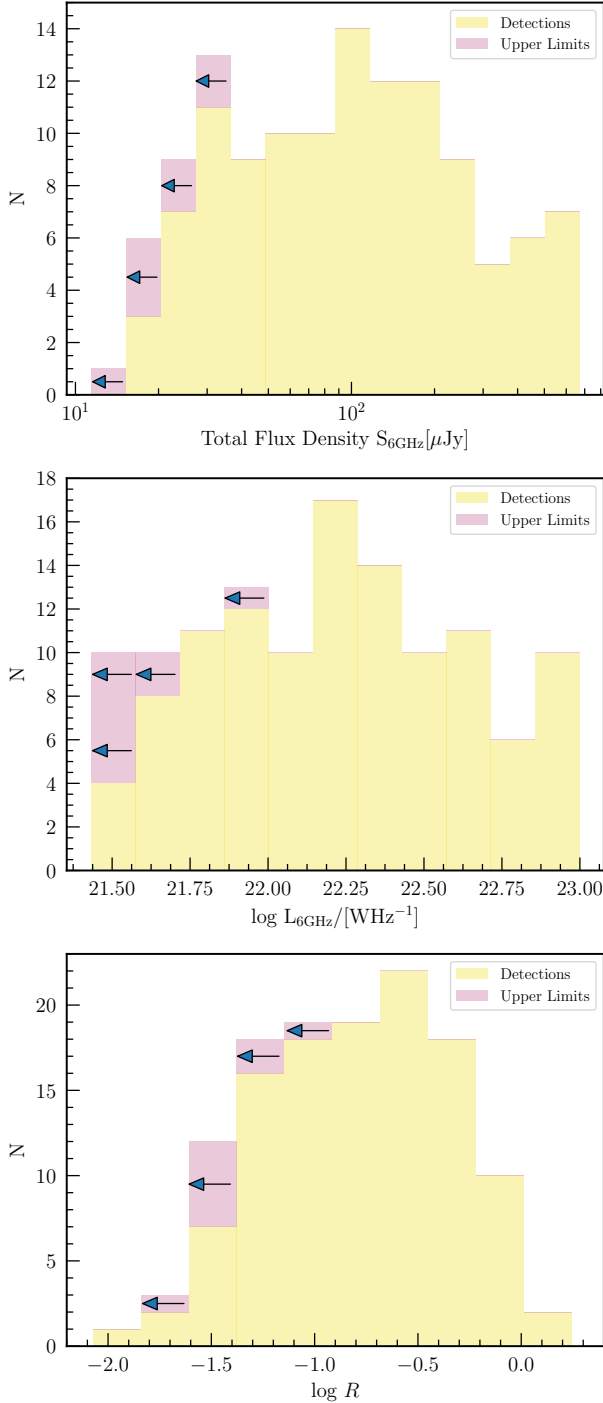


**Figure 2.** Distributions of the radio properties of targets in our sample observed at  $\sim 0.33''$  resolution. Top: total 6 GHz flux density measured with the VLA. Middle: total 6 GHz luminosity. Bottom: base-10 logarithm of  $R$ , where  $R$  represents the ratio between our measured 6 GHz flux density and the source’s optical  $i$ -band flux density (Schneider et al. 2010).

regarding the nature of radio emission throughout the RQQ population. Certain morphologies may give more inclination towards certain origins of radio emission than the other, potentially much in the way that we can simply look at a RL quasar and view that AGN-powered jets are the dominant origin.

While Kellermann et al. (1994) showed that some compact RQQ structures have been resolved by moving to higher resolution follow-up observations from Kellermann et al. (1989), hinting at RQQs simply being scaled down versions of RLQs, there are many problems with that investigation. For starters, the Palomar-Green Bright Quasar Survey (BQS; Schmidt & Green 1983) provides the sample selection for that paper, but the well-known biases of the BQS (e.g., Jester et al. 2005) prevent obtaining a homogeneous sample that is truly representative of the entire known QSO population. Furthermore, their limited sensitivity meant that they were only able to reach high enough signal-to-noise to even investigate the possibility of extended structure in some 10 of all of their RQQs—and even that will only concern the brightest of all their RQQs, many of which properly qualify as radio-intermediate by our standards (see Section 2 for a definition of “radio-quiet”).

Our unprecedented sensitivity in A-configuration together with the advancements of new sophisticated source-finding algorithms (PyBDSF), allows us to investigate the possibility of low-surface-brightness extended structures across our entire volume-limited sample of RQQs. We find that there are a number of morphologies that RQQs possess on our resolution scales and adopt the following shorthand to classify our sources:

- **U**—*Unresolved*: the source remains unresolved on A-configuration scales ( $\sim 1.3\text{kpc}$  at  $z \sim 0.25$ ). A total of 63 of our sources remain unresolved.
- **SR**—*Slightly Resolved*: the source shows some resolution beyond the synthesized beam, hinting at slight extended structure of the order  $\sim 1.3\text{kpc}$ . 32 sources fall into this category.
- **M**—*Multi-component*: the source has a component coinciding with the SDSS optical position of the QSO, and also has one or more compact components contributing to the source’s total radio emission. 13 sources are defined by this morphology.
- **E**—*Extended*: the source has obvious extended emission extending well beyond the resolution of the synthesized beam. 8 of our sources demonstrate clear extended morphology.
- **D**—*Double*: there are two apparent radio “lobes” symmetrically straddling the central QSO position. There is only one lone RQQ that has a double morphology in our sample (J0935+4819; see the top left image in Figure 3).

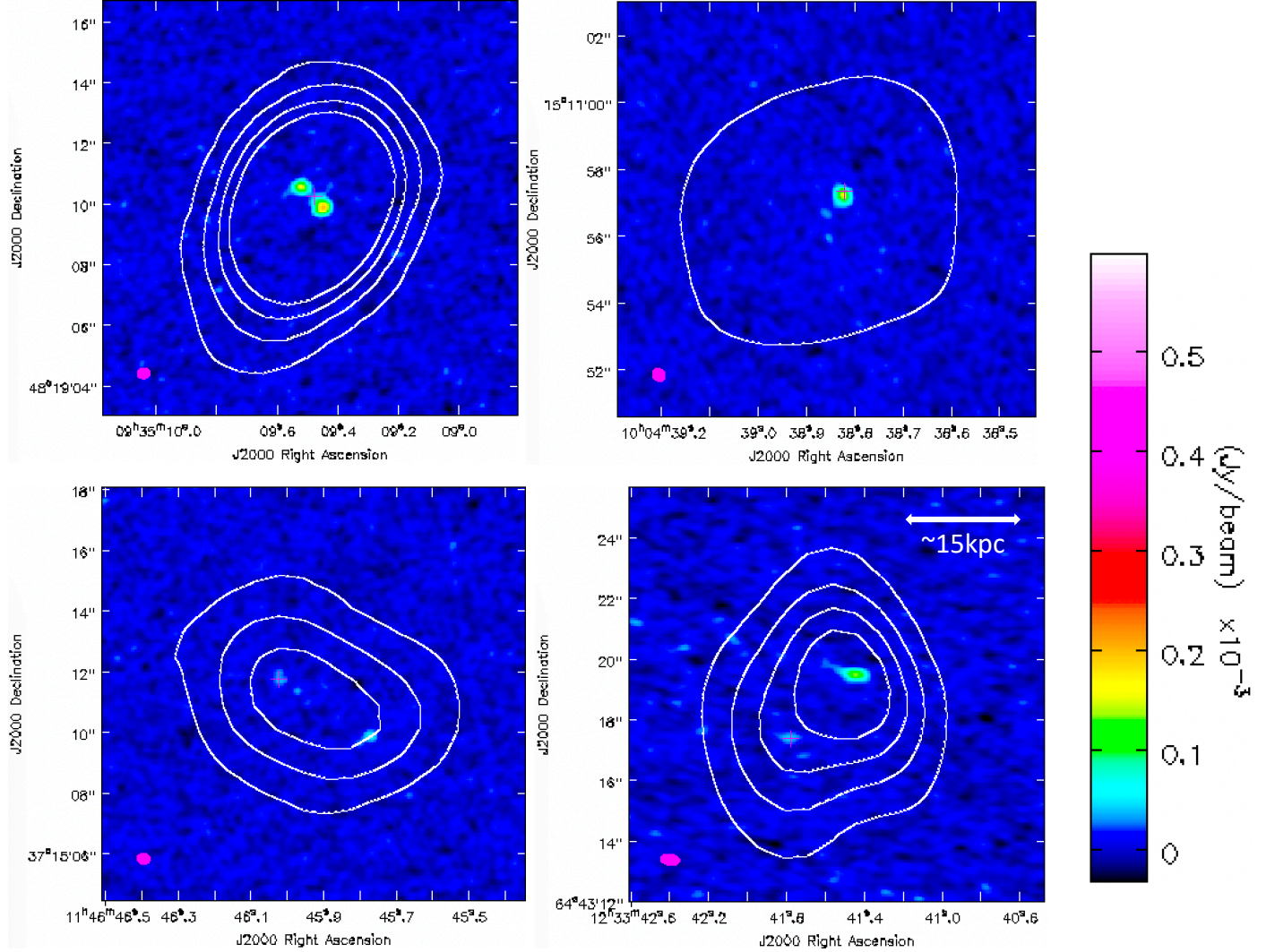


**Figure 3.** Images ( $\sim 12'' \times 12''$ ) of RQQs with complex radio morphologies in our sample. Contours are scaled in all images so that the outermost contour represents the boundary of the unresolved source imaged in Kellermann et al. (2016). The SDSS optical position of the QSO is represented by a small magenta cross (typical  $\sim 0.1''$  uncertainties). The FWHM of the synthesized beam for each observation is indicated by the filled magenta ellipse in the lower left-hand corner of each image. An approximate linear size scale is given in the bottom right image. Top left: J0935+4819, our lone source with a “Double” (D) radio morphology; it is difficult (if possible) to parse how a physical origin such as star formation could produce such a morphology. Top left: J1004+1510, a multi-component (M) source where the dominant component is aligned with the optical position of the QSO, and two fainter compact components also contribute to the source’s overall luminosity. Bottom right: J1146+3715, another multi-component source; interestingly, the two oddly-shaped points of emission towards the upper left of the image overlap with the optical position of the QSO, while the brighter, more well-defined point of emission towards the lower right is offset  $\sim 15\text{kpc}$  away from the QSO. Bottom right: J1233+6443, inspection of the SDSS optical image (Abazajian et al. 2009) suggests that the QSO (fainter source slightly offset down and to the left) may be interacting with another galaxy (the bright source slightly up and to the right).

- **ND—Non-detection:** no potential radio component from the source is detected above  $3\text{-}\sigma_{\text{rms}}$ ; typically, upper limits for non-detections in our sample are  $\sim 21\mu\text{Jy}$  (corresponding to  $\sim 10^{21.6}\text{W Hz}^{-1}$  at  $z \sim 0.25$ ), but vary slightly depending on depth reached in each observation, with our deepest observation (J1703+1910) achieving an upper

limit of  $13.2\mu\text{Jy}$  ( $\sim 10^{21.4}\text{W Hz}^{-1}$ ). Only 6 total sources are not detected in our A-configuration observations.

Exemplary images from the different morphology categories are presented in Figures 3 and 4. While virtually all RQQs were unresolved on previous C-configuration scales, we find that at our higher resolution, the sample

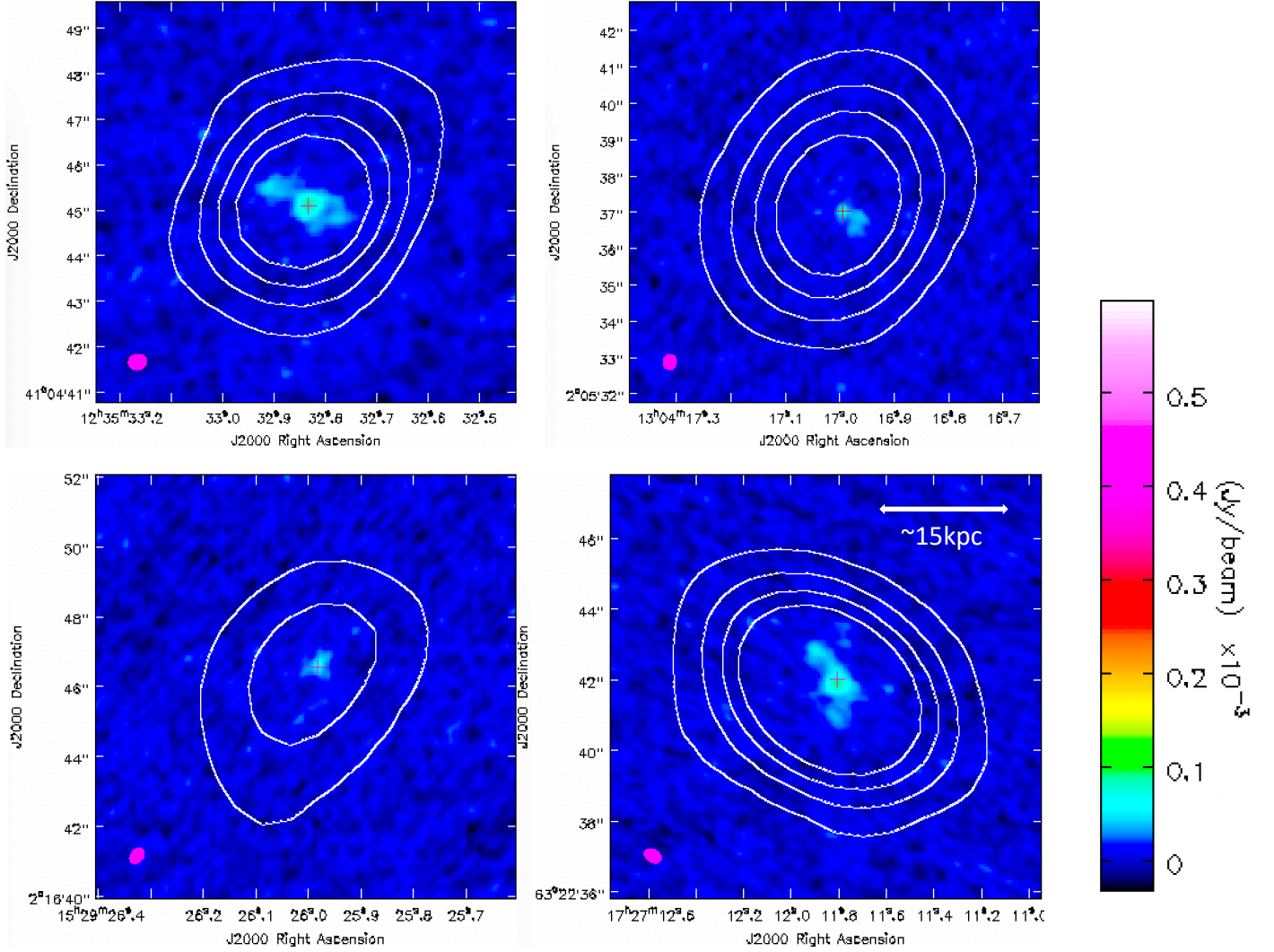


**Figure 4.** Images ( $\sim 12'' \times 12''$ ) of RQQs with complex radio morphologies in our sample. Contours are scaled in all images so that the outermost contour represents the boundary of the unresolved source imaged in Kellermann et al. (2016). The SDSS optical position of the QSO is represented by a small magenta cross (typical  $\sim 0.1''$  uncertainties). The FWHM of the synthesized beam for each observation is indicated by the filled magenta ellipse in the lower left-hand corner of each image. An approximate linear size scale is given in the bottom right image. Top left: J1235+4104, an RQQ with a typical “Extended” morphology (**E**) in our sample. Top right: J1304+0205, the faintest source ( $L_{6\text{GHz}} \sim 10^{22.5} \text{W Hz}^{-1}$ ) that we detect clear extended emission in. Bottom left: J1529+0216, an example of what typically qualifies as a “slightly resolved” (**SR**) radio source. Bottom right: J1727+6322, another example of an extended morphology RQQ in our sample. Contours are scaled so that the outermost contour represents the boundary of the unresolved source imaged in Kellermann et al. (2016).

is permeated with each of the other five morphologies. Roughly 41% of all RQQs in this sample show some complex structure  $\gtrsim 1.3\text{kpc}$  from the centers of their host galaxies. Luminosity distributions for the different morphology classes are shown in Figure 5, where we see that the lower-power sources are dominated by unresolved morphology, with the complex sources shaping the brighter end of the RQQ population.

#### 4.2. Resolution Effects

The diffraction limitations of interferometers offer a significant scientific advantage in interpreting our follow-

up A-configuration observations. By moving from  $3.5''$  to  $0.33''$  resolution, our largest angular scale detectable in the C-band has also decreased. Hence, if there were some diffuse, extended emission present within  $3.5''$  of the QSO that is undetected by the VLA in its A-configuration, we will have effectively resolved out flux in our observation, and there are only specific origins of radio emission that would predict such a behavior.

Specifically, star formation processes across host galaxies fit this profile. Supernova remnants (SNRs) emerge kiloparsecs from their home star and accelerate electrons throughout the host galaxy of the QSO, which then emit

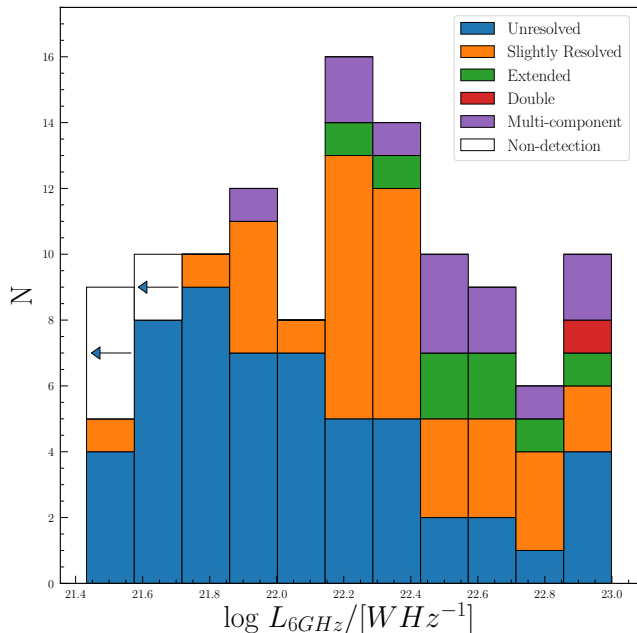


**Figure 5.** 6 GHz luminosity distributions of different morphologies present in our sample.

synchrotron radiation (see Condon 1992, and references therein for a review on radio emission in galaxies), which is the theorized added contributor of radio emission in RQQs. While supernova radio emission may begin on compact scales near that of the originating star, the emission from the radiating electrons will long outlive the SNR and form something of a “soup” of radio emission spread throughout the host galaxy that may be filtered out by the VLA’s A-configuration.

To test this effect, we estimate to what extent our flux density measurements from A-configuration systematically decrease from previous C-configuration observations from Kimball et al. (2011). If all sources were completely non-variable and we were not resolving out any emission in A-configuration, then we would simply expect the ratio between the measured flux density in C-configuration from Kellermann et al. (2016) and that measured in this paper to be 1.0 for all sources. However, that is very clearly not what we see; Figure 6 shows the distribution of the ratio between our measured 6 GHz flux density and that measured in Kellermann et al. (2016). The sheer spread of this distribution alone tells us that our sources are variable, at least to some extent—we have plenty of sources that both decrease in flux density from 2011, as well as ones that increase, which is a trademark property of variability in QSOs [Hovatta+2007]. While this fact that our sources are inherently variable complicates what we are trying to express, we can still statistically determine what fraction of our sources are subject to notable resolution effects, and thus which sources likely have a significant amount

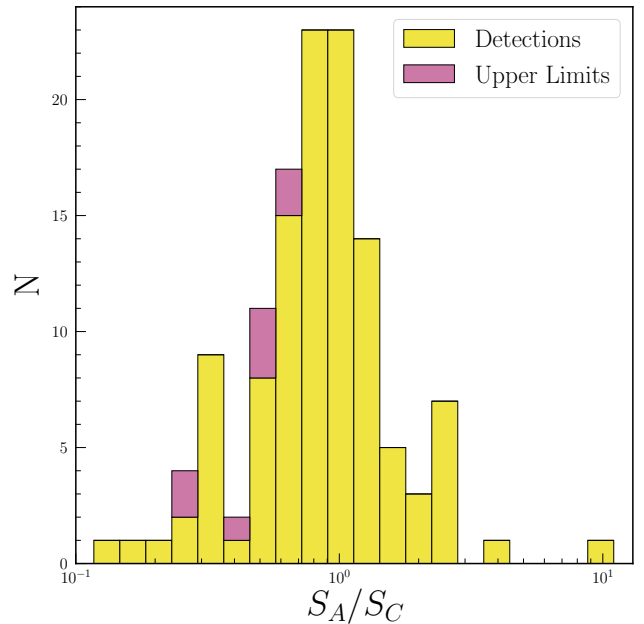


**Figure 6.** Distribution of flux ratio between our A-configuration ( $\sim 0.33''$ ) observations and C-configuration ( $\sim 3.5''$ ) flux densities measured in Kellermann et al. (2016). The slight leftward skew and offset from unity indicate that changes in flux density must be due at least in part to resolution effects.

of star formation contributing to their total radio luminosity.

The median ratio between flux densities measured in this paper and in Kellermann et al. (2016) is 0.85, implying that we are indeed resolving out emission throughout our sample. To dig deeper into how many of our sources may be significantly affected by *this specifically* (and not just variability), we first fit a lognormal distribution to our flux ratio histogram and perform a  $1\text{-}\sigma$  cutoff to define the sources in the center of the plot; all of the fractional changes in flux density among these sources are small enough such that we can attribute slight changes to variability, or even small differences in flux density measurement between the two observing campaigns. We then look at the sources outside this  $1\text{-}\sigma$  cutoff; if variability was the only cause of changes in flux density, we expect that of a source to be just as likely to increase as it is to decrease, so the counts on each side of this cutoff should roughly agree. What we actually see is 37% of sources falling below this  $-\sigma$  cutoff, with only 25% of sources rising above the  $+\sigma$  cutoff. We then conclude that  $\approx 12\%$  of our observed sources are affected by the higher resolution of the VLA’s A-configuration.

It is perhaps more enlightening to look at the distribution of such a ratio as a function of different radio morphologies. RQQs are not simply a single class of objects, so there may be significant differences in the

presence (or dimensions) of star-formation-like emission in various flavors of RQQs. Indeed, we see that in Figure 7, we are resolving out much more emission in the sources named “unresolved” compared to all other morphologies.

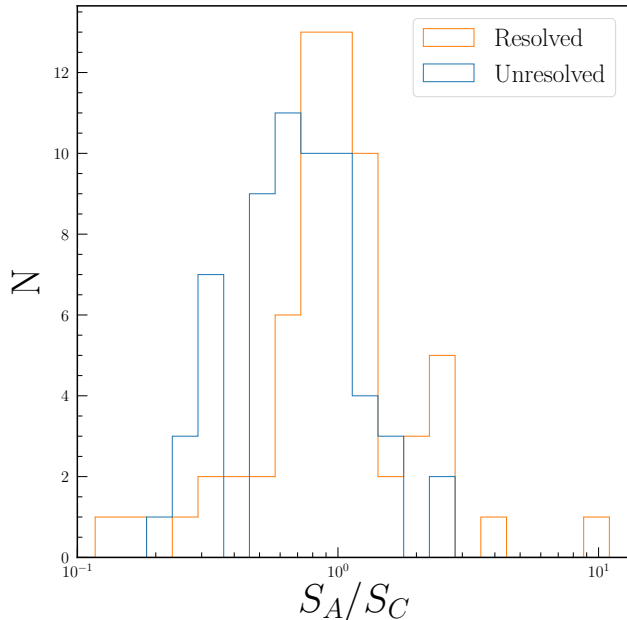


**Figure 7.** Distribution of flux ratio between our A-configuration ( $\sim 0.33''$ ) observations and C-configuration ( $\sim 3.5''$ ) flux densities measured in Kellermann et al. (2016), considering unresolved and resolved sources separately. The unresolved sources (median  $\sim 0.74$ ) exhibit much more significant resolution effects than the resolved sources (median  $\sim 0.91$ ).

The fact that the sources that remain unresolved in our observations systematically decreased *more* than the resolved sources reveals important information about the fainter end of our population. If a source remained unresolved even at our higher resolution and its flux density roughly agreed with its previous observation (ignoring variability), then we could conclude that all of the flux detected in C-configuration was simply confined to a core component much smaller than that of the  $\sim 3.5''$  C-configuration synthesized beam. However, because their fractional decreases in flux densities are markedly higher than what is measured in the resolved sources, we are surely resolving out emission in these targets.

An explanation for this result could be that these weaker sources really do have extended structures—all of their flux is not simply confined to the detected unresolved core—but our sensitivity is simply not sufficient to detect their potentially extremely low surface brightness. Indeed, Blundell & Rawlings (2001) revealed faint FRI-like structure (Fanaroff & Riley 1974) in a high op-

tical luminosity QSO whose radio emission appeared to be dominated by a single core, but deep radio imaging revealed otherwise. It may also be possible that star-formation-related emission is being resolved out, and star formation spread throughout host galaxies is only largely prevalent in the fainter RQQs.

#### 4.3. Variability

It is well known that RLQs exhibit variability on timescales of years, months, and even days (Barvainis et al. 2005; Hovatta et al. 2007; Thyagarajan et al. 2011), due presumably to the source of radio emission in such objects being an optically opaque, compact engine intimately associated with the AGN. To see if the same effects were spread throughout quasars across the full radio-loudness spectrum, Barvainis et al. (2005) simultaneously studied samples of 11 RLQs, 11 RIQs, and 11 RQQs over 10 different observing epochs, with a spacing of roughly 2 weeks to 2 months between each observation (with the final two epochs spaced 18 months apart), amounting to  $\sim 2$  total years spanned in observing for each source. They concluded that similarities in the radio light curves between all three classes of objects, coupled with the presence of flat spectral indices throughout the RQ sources meant that the underlying physics driving the radio emission in RQQs must be the same as in RLQs. However, Condon et al. (2013) found a stark contrast to the spectral index conclusion, wherein they found, through a statistical analysis of NVSS data, that the typical radio spectral index for low-redshift ( $0.2 < z < 0.45$ ) RQQs is actually  $\alpha \approx -0.7$ . Such a dramatic difference in spectral index requires *different physics* to be occurring around the inner region of each type of QSO.

Nyland et al. (2020) examined a sample of 26 quasars that were determined to be radio-quiet based on upper limits in the FIRST survey (1993–2003; Becker et al. 1995), but have since been detected based on “Quick Look” (QL) images from Epoch 1 of the VLA Sky Survey (VLASS1.1/2 observations span 2017–2019; Lacy et al. 2020), and so have now transitioned into a clear radio-loud state. Thus, the cadence of our 2010/11 observations in Kimball et al. (2011) and 2019 observations in this paper should be a good fit for both observing how the radio luminosities of RQQs may vary on decadal timescales in their “typical” state, while also roughly giving each individual quasar enough time to undergo any significant changes that may occur over the timespan of our observations.

To lengthen the time domain of our light curves, we also make use of FIRST data (Becker et al. 1995). While most RQQs are typically not listed as sources in the final FIRST catalog, many of our targets are bright enough at low enough redshift such that they appear as faint  $\lesssim 5\text{-}\sigma_{\text{FIRST}}$  detections, where  $\sigma_{\text{FIRST}} \approx 0.15\text{mJy bm}^{-1}$ . 29 of our total 124 RQQs qualify as faint detections in

FIRST, and we consider this subset of our sample to study the variability of RQQs.

We also reintroduce the radio-intermediate (27 RIQs) and -loud (14 RLQs) samples of quasars from [Kimball et al. \(2011\)](#) and [Kellermann et al. \(2016\)](#). We only consider the cores of extended RI and RL quasars as RQQs do not have large-scale lobes or jets, and such structures are not thought to be variable over decadal timescales in any case ([Blandford et al. 2019](#)). Since we do not have 2019 A-configuration observations of these quasars, we instead follow [Nyland et al.](#) and retrieve QL images from VLASS Epoch 1 to get *S*-band data of each of these targets at roughly the same timestamp as of our A-configuration observations of RQQs. While these QL images do not constitute the final data products of VLASS and inherently possess uncertainties up to  $\sim 20\%$ , these potential errors are small enough so as to not change our final conclusions in this part of our analysis.

While any FIRST/VLASS data we can obtain for each target is undoubtedly valuable to our investigation, there is one caveat to using these results: FIRST (*L*-band) and VLASS (*S*-band) give us flux densities at different observed frequencies than our *C*-band observations. We can't simply utilize the FIRST data to compute a spectral index from *L*- to *C*-band, because such an operation would rely on the assumption that our sources are not variable, which is easily refuted by the spread seen in [Figure 6](#). As such, we must adopt either a steep ( $\alpha = -0.7$ ) or flat ( $\alpha = 0.0$ ) radio spectral index to convert FIRST and VLASS measurements to our preferred 6 GHz reference frequencies. This is an important decision because the difference in choice of spectral index yields a difference in 6 GHz spectral luminosity of roughly 0.37 dex for FIRST sources, and 0.14 dex for VLASS sources.

Given the conflicting results in the literature regarding spectral indices in different-power QSOs, we can not reasonably employ a choice of  $\alpha$  without controversy of the results; we can, however, use both choices of spectral index, and statistically determine which choice more accurately reflects our *a priori* assumptions on what we'd expect the radio light curves of variable QSOs to look like.

The 6 GHz light curves for each case of  $\alpha$  are shown in [Figure 8](#). By viewing all curves plotted together, we can already see some systemic effects as a result of choice of spectral index. Specifically, for the RQQ data obtained assuming  $\alpha = 0.0$ , there is no physical reason to think that all of our sources would systematically decrease in luminosity from FIRST timespans to the 2010/11 observations with the VLA ([Kimball et al. 2011](#)), so even this preliminary check across all sources suggests that RQQs are likely to have steep spectral indices rather than flat. To further investigate which choice of spectral index better matches each *individual* QSO, we assume that the radio luminosity of any QSO should change as a power

law over the decadal timescales we consider. We then fit a power law to the light curve of each source for each case of  $\alpha$ , and perform a reduced  $\chi^2$  goodness-of-fit test on each case to determine which spectral index provides a better match to our assumed power law model. We find that 19/29 (65.5%) RQQs and 19/27 (70.4%) RIQs are well-suited by a steep spectral index ( $\alpha = -0.7$ ), and the RLQs sharply contrast this, with 12/14 (85.7%) of their light curves being better modeled by a flat spectral index ( $\alpha = 0.0$ ). RQQ light curves that were better matched to  $\alpha = 0.0$  based on  $\chi^2$  are likely biased towards sources whose flux density decreased in A-configuration observations due mostly to resolution effects, so the number of RQQs with  $\alpha = -0.7$  is seemingly a fair amount higher than our statistics suggest.

Our results imply at least two separate QSO populations with different dominant sources of radio power in each population: the RL cores are dominated by flat spectrum radio emission from an optically opaque core associated with the AGN, and the RQ cores are dominated by steep spectrum synchrotron emission, either from weak/frustrated or nascent jets ([Nyland et al. 2020](#)), or starburst activity ([Condon 1992](#)). Whatever the physical origin of synchrotron emission in RQQs, it must be something that fits the timescales that RQQs are observed to be variable over. It is not currently thought that starburst emission can be significantly variable over the  $\sim 1.3$ kpc that our A-configuration synthesized beam samples, although we cannot ignore the possibility of there being a mixture of AGN and starburst activity contributing to the total radio luminosity ([Kimball et al. 2011](#)), with the AGN contribution being the primary cause of variability. However, fractional increases in flux density of  $\gtrsim 100\%$  in J0822+4553, J1000+1047, J1617+0638, and J1627+4736 indicate that a starburst would only be contributing slightly (if at all) to the observed radio, at least in those RQQs. Future investigations monitoring the optical spectroscopy of RQQs in parallel with their observed radio variability would help shed light on the question of whether or not the origin of this radio activity is intrinsic to the AGN (e.g., due to enhancements of accretion activity [Kunert-Bajraszewska et al. 2020](#)). While nascent or receding jets could explain some of the extended morphologies throughout our targets, VLBI imaging techniques are needed to confirm the presence or absence of parsec-scale radio jets in RQQs. While [Ulvestad et al. \(2005\)](#) and [Herrera Ruiz et al. \(2016\)](#) have used VLBI to detect such jets in small numbers of radio-selected claimed RQQs, many detections in their samples properly qualify as either radio-intermediate or -loud, so we would expect a significant jet contribution in those objects and it is not clear how those results translate to our sample of firmly radio-quiet sources. VLBI detections of jets in the RQQs spread throughout our sample would, however, align with their claims that what drives the radio

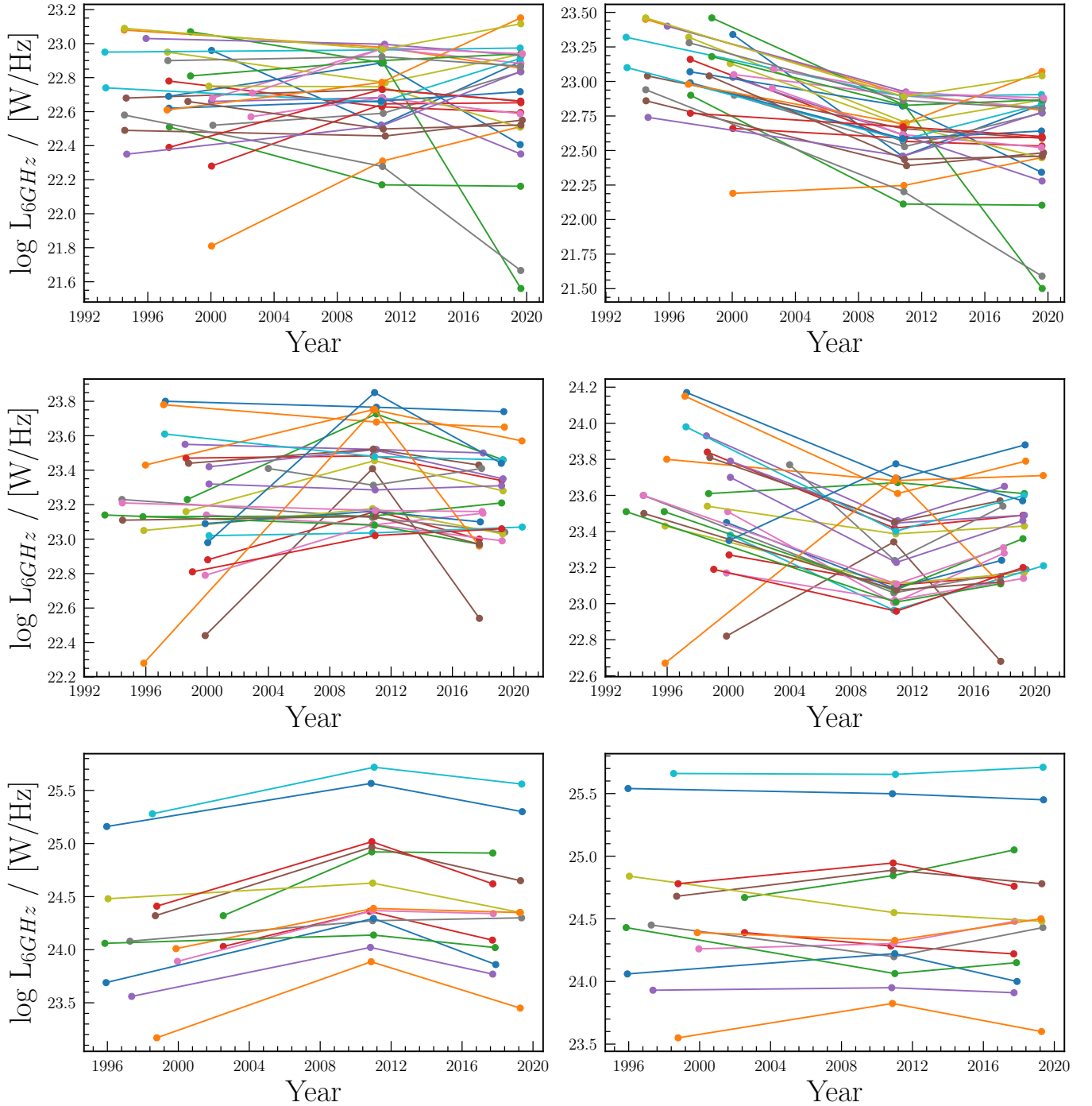


**Figure 8.** Light curves of all QSOs considered in our variability analysis. The top panel shows the curves of the 29 RQQs examined, the middle panel shows the 27 RIQs, and the bottom the 14 RLQs. The left column shows the resultant curves assuming a steep spectral index ( $\alpha = -0.7$ ) in converting FIRST and VLASS flux densities to our 6 GHz observing frequency, while the right-hand column shows the resultant curves assuming a flat spectral index ( $\alpha = 0.0$ ). FIRST observations span 1993–2003; all 2010/11 points reflect data from [Kellermann et al. \(2016\)](#); for the RQQs, the 2019 data points represent flux densities from this paper; the 2017–2019 data points for the RIQs and RLQs reflect data from preliminary “Quick Look” images from Epoch 1 of VLASS. Error bars only deviate inordinately from point sizes in the case of VLASS, where up to 20% errors in flux density correspond to lower limits of  $-0.10$  dex and upper limits of  $+0.08$  dex on a logarithmic scale.

emission seen in RQQs is ultimately very similar to what drives it in RLQs.

## 5. CONCLUSIONS

We have performed a comprehensive study of the low-redshift ( $0.2 < z < 0.3$ ) radio-quiet QSO population (124 RQQs) from the homogeneous, optically selected, volume-limited sample of 178 QSOs studied in [Kimball et al. \(2011\)](#) and [Kellermann et al. \(2016\)](#). We performed these observations in the VLA’s A-configuration, which yielded a typical angular resolution of  $\sim 0.33''$  ( $\sim 1.3\text{kpc}$  at  $z = 0.25$ ) at our 6 GHz observing frequency, which then allowed us to detect complex subgalactic radio morphologies in at least  $\sim 41\%$  of the RQQs studied herein (see Section 4.1 for coverage on radio morphologies); these sources are typically brighter than the sources that are unresolved on the  $0.33''$  scale. We also found that the median flux density of the RQQs measured in this paper decreased  $\approx 15\%$  from the median measured in [Kellermann et al. \(2016\)](#), indicating the presence of diffuse extended emission throughout our sample. Moreover, these systematic decreases in flux density are much more prevalent among the fainter unresolved sources in our sample. This simple result can mean one of two things: either star formation is being filtered out through our transition to A-configuration and is a much more significant contributor to the total radio luminosity in the fainter end of the RQQ population, or these fainter (apparently unresolved) sources really do have extended emission, but the extended structures are just much too low surface brightness to actually detect within our observing time.

We also utilized FIRST ([Becker et al. 1995](#)) and “Quick Look” images from Epoch 1 of the ongoing VLA Sky Survey ([Lacy et al. 2020](#)) to construct 6 GHz light curves of a subset of 29 of our RQQs, as well as 27 RIQs and 14 RLQs from the full [Kimball et al. \(2011\)](#) sample. We found that the light curves between the radio-quiet, -intermediate, and -loud sources are essentially indistinguishable, agreeing with the findings of [Barvainis et al. \(2005\)](#). However, we also find that by assuming that the light curve of each source studied should vary roughly as a power law over the decadal timescales we consider,

that the typical spectral index for the radio-quiet sources is steep ( $\alpha \approx -0.7$ ), while the typical spectral index for the cores of the radio-loud objects is flat ( $\alpha \approx 0.0$ ), indicating that the underlying physics occurring within the inner kiloparsec-scale regions of RQQs and RLQs must ultimately be different (see Section 4.3 for further discussion on this analysis). These findings agree with other sources in the literature (e.g., [Condon et al. 2013](#)), and such physical origins that could explain the observed variability and spectral shapes include a mixture of synchrotron emission from a starburst and AGN activity ([Kimball et al. 2011](#)), as well as possible nascent or receding jets ([Nyland et al. 2020](#)), which could explain the complex extended morphologies we see in some of our sources.

#### ACKNOWLEDGMENTS

Trevor McCaffrey is a student at the National Radio Astronomy Observatory. The National Radio Astronomy Observatory is a facility of the National Science Foundation operated under cooperative agreement by Associated Universities, Inc. Trevor McCaffrey acknowledges support from the “Research Experiences for Undergraduates” program of the National Science Foundation.

This research has made use of NASA’s Astrophysics Data System Bibliographic Services.

This research has made use of the VLASS QImage cutout server at URL <http://206.12.91.186/>, operated by the Canadian Initiative for Radio Astronomy Data Analysis (CIRADA). CIRADA is funded by a grant from the Canada Foundation for Innovation 2017 Innovation Fund (Project 35999), as well as by the Provinces of Ontario, British Columbia, Alberta, Manitoba and Quebec, in collaboration with the National Research Council of Canada, the US National Radio Astronomy Observatory and Australia’s Commonwealth Scientific and Industrial Research Organisation.

#### REFERENCES

- Abazajian, K. N., Adelman-McCarthy, J. K., Agüeros, M. A., et al. 2009, *ApJS*, 182, 543, doi: [10.1088/0067-0049/182/2/543](https://doi.org/10.1088/0067-0049/182/2/543)
- Barvainis, R., Lehar, J., Birkinshaw, M., Falcke, H., & Blundell, K. M. 2005, *ApJ*, 618, 108, doi: [10.1086/425859](https://doi.org/10.1086/425859)
- Becker, R. H., White, R. L., & Helfand, D. J. 1995, *ApJ*, 450, 559, doi: [10.1086/176166](https://doi.org/10.1086/176166)
- Blandford, R., Meier, D., & Readhead, A. 2019, *ARA&A*, 57, 467, doi: [10.1146/annurev-astro-081817-051948](https://doi.org/10.1146/annurev-astro-081817-051948)
- Blundell, K. M., & Rawlings, S. 2001, *ApJL*, 562, L5, doi: [10.1086/337970](https://doi.org/10.1086/337970)
- Condon, J. J. 1992, *ARA&A*, 30, 575, doi: [10.1146/annurev.aa.30.090192.003043](https://doi.org/10.1146/annurev.aa.30.090192.003043)
- Condon, J. J., Cotton, W. D., Greisen, E. W., et al. 1998, *AJ*, 115, 1693, doi: [10.1086/300337](https://doi.org/10.1086/300337)
- Condon, J. J., Kellermann, K. I., Kimball, A. E., Ivezić, Ž., & Perley, R. A. 2013, *ApJ*, 768, 37, doi: [10.1088/0004-637X/768/1/37](https://doi.org/10.1088/0004-637X/768/1/37)
- Cornwell, T. J., Golap, K., & Bhatnagar, S. 2005, in *Astronomical Society of the Pacific Conference Series*, Vol. 347, *Astronomical Data Analysis Software and Systems XIV*, ed. P. Shopbell, M. Britton, & R. Ebert, 86
- Fanaroff, B. L., & Riley, J. M. 1974, *MNRAS*, 167, 31P, doi: [10.1093/mnras/167.1.31P](https://doi.org/10.1093/mnras/167.1.31P)
- Giustini, M., & Proga, D. 2019, *A&A*, 630, A94, doi: [10.1051/0004-6361/201833810](https://doi.org/10.1051/0004-6361/201833810)

- Herrera Ruiz, N., Middelberg, E., Norris, R. P., & Maini, A. 2016, *A&A*, 589, L2, doi: [10.1051/0004-6361/201628302](https://doi.org/10.1051/0004-6361/201628302)
- Hovatta, T., Tornikoski, M., Lainela, M., et al. 2007, *A&A*, 469, 899, doi: [10.1051/0004-6361:20077529](https://doi.org/10.1051/0004-6361:20077529)
- Jagannathan, P., Bhatnagar, S., Brisken, W., & Taylor, A. R. 2018, *AJ*, 155, 3, doi: [10.3847/1538-3881/aa989f](https://doi.org/10.3847/1538-3881/aa989f)
- Jester, S., Schneider, D. P., Richards, G. T., et al. 2005, *AJ*, 130, 873, doi: [10.1086/432466](https://doi.org/10.1086/432466)
- Kellermann, K. I., Condon, J. J., Kimball, A. E., Perley, R. A., & Ivezić, Ž. 2016, *ApJ*, 831, 168, doi: [10.3847/0004-637X/831/2/168](https://doi.org/10.3847/0004-637X/831/2/168)
- Kellermann, K. I., Sramek, R., Schmidt, M., Shaffer, D. B., & Green, R. 1989, *AJ*, 98, 1195, doi: [10.1086/115207](https://doi.org/10.1086/115207)
- Kellermann, K. I., Sramek, R. A., Schmidt, M., Green, R. F., & Shaffer, D. B. 1994, *AJ*, 108, 1163, doi: [10.1086/117145](https://doi.org/10.1086/117145)
- Kimball, A. E., Kellermann, K. I., Condon, J. J., Ivezić, Ž., & Perley, R. A. 2011, *ApJL*, 739, L29, doi: [10.1088/2041-8205/739/1/L29](https://doi.org/10.1088/2041-8205/739/1/L29)
- Kunert-Bajraszewska, M., Wołowska, A., Mooley, K., Kharb, P., & Hallinan, G. 2020, *ApJ*, 897, 128, doi: [10.3847/1538-4357/ab9598](https://doi.org/10.3847/1538-4357/ab9598)
- Lacy, M., Baum, S. A., Chandler, C. J., et al. 2020, *PASP*, 132, 035001, doi: [10.1088/1538-3873/ab63eb](https://doi.org/10.1088/1538-3873/ab63eb)
- McMullin, J. P., Waters, B., Schiebel, D., Young, W., & Golap, K. 2007, in *Astronomical Society of the Pacific Conference Series*, Vol. 376, *Astronomical Data Analysis Software and Systems XVI*, ed. R. A. Shaw, F. Hill, & D. J. Bell, 127
- Nyland, K., Dong, D., Patil, P., et al. 2020, arXiv e-prints, arXiv:2005.04734. <https://arxiv.org/abs/2005.04734>
- Rau, U., & Cornwell, T. J. 2011, *A&A*, 532, A71, doi: [10.1051/0004-6361/201117104](https://doi.org/10.1051/0004-6361/201117104)
- Richards, G. T., Fan, X., Newberg, H. J., et al. 2002, *AJ*, 123, 2945, doi: [10.1086/340187](https://doi.org/10.1086/340187)
- Schmidt, M. 1963, *Nature*, 197, 1040, doi: [10.1038/1971040a0](https://doi.org/10.1038/1971040a0)
- Schmidt, M., & Green, R. F. 1983, *ApJ*, 269, 352, doi: [10.1086/161048](https://doi.org/10.1086/161048)
- Schneider, D. P., Richards, G. T., Hall, P. B., et al. 2010, *AJ*, 139, 2360, doi: [10.1088/0004-6256/139/6/2360](https://doi.org/10.1088/0004-6256/139/6/2360)
- Thyagarajan, N., Helfand, D. J., White, R. L., & Becker, R. H. 2011, *ApJ*, 742, 49, doi: [10.1088/0004-637X/742/1/49](https://doi.org/10.1088/0004-637X/742/1/49)
- Ulvestad, J. S., Antonucci, R. R. J., & Barvainis, R. 2005, *ApJ*, 621, 123, doi: [10.1086/427426](https://doi.org/10.1086/427426)
- Wright, E. L. 2006, *PASP*, 118, 1711, doi: [10.1086/510102](https://doi.org/10.1086/510102)
- Zakamska, N. L., & Greene, J. E. 2014, *MNRAS*, 442, 784, doi: [10.1093/mnras/stu842](https://doi.org/10.1093/mnras/stu842)
- Zakamska, N. L., Lampayan, K., Petric, A., et al. 2016, *MNRAS*, 455, 4191, doi: [10.1093/mnras/stv2571](https://doi.org/10.1093/mnras/stv2571)

## APPENDIX

## A. RADIO DATA

Data in Table 1 is listed as follows:

- **Column 1:** Abbreviated target name in Jhhmm+ddmm format
- **Column 2:** Peak 6 GHz flux densities from the VLA at  $\sim 0.33''$  resolution with uncertainties computed by the imfit task in CASA
- **Column 3:** Total 6 GHz flux densities from the VLA at  $\sim 0.33''$  resolution with uncertainties computed by the imfit task in CASA
- **Column 4:** Ratio between the peak flux measured in column 2 and the total measured in column 3
- **Column 5:** Ratio between our measured total 6 GHz flux density at  $0.33''$  and that measured at  $3.5''$  in [Kellermann et al. \(2016\)](#)
- **Column 6:** Base-10 logarithm of 6 GHz luminosity
- **Column 7:** Targets' radio morphology at  $0.33''$  determined by eye (see Section 4.1 for a description of morphologies)

**Table 1.** Target Quasar Radio Properties

(1)	(2)	(3)	(4)	(5)	(6)	(7)
Name	$S_p$	$S_{\text{tot}}$	$S_p/S_{\text{tot}}$	$S_A/S_C$	$\log L_{6\text{GHz}}$	Morph.
(Jhhmm+ddmm)	$\mu\text{Jy bm}^{-1}$	$\mu\text{Jy}$			( $\text{W Hz}^{-1}$ )	A-config.
J0808+4407	$36.3 \pm 8.3$	$36.3 \pm 8.3$	1.00	0.60	21.90	U
J0816+4258	$179.0 \pm 7.4$	$199.0 \pm 14.0$	0.90	0.86	22.49	SR
J0822+4553	$425.0 \pm 10.0$	$531.0 \pm 33.0$	0.80	2.39	23.15	M
J0834+3826	$117.0 \pm 7.1$	$117.0 \pm 7.1$	1.00	0.91	22.45	U
J0843+5357	$123.0 \pm 8.2$	$349.0 \pm 31.0$	0.35	0.85	22.66	E
J0847+2631	$27.0 \pm 2.7$	$41.0 \pm 6.3$	0.66	2.44	21.98	SR
J0858+3423	$104.0 \pm 8.8$	$189.0 \pm 24.0$	0.55	0.90	22.55	M
J0904+5114	$26.6 \pm 6.8$	$26.6 \pm 6.8$	1.00	0.85	21.74	U
J0907+0215	$20.3 \pm 2.3$	$20.3 \pm 2.3$	1.00	0.58	21.64	U
J0923+4530	$56.4 \pm 8.9$	$56.4 \pm 8.9$	1.00	0.66	22.15	U
J0929+4644	$76.4 \pm 6.8$	$76.4 \pm 6.8$	1.00	0.60	22.09	U
J0934+0306	$31.5 \pm 0.0$	$31.5 \pm 0.0$	1.00	0.44	21.91	SR
J0935+4819	$194.0 \pm 17.0$	$528.0 \pm 47.0$	0.37	0.88	22.87	D
J0942+3451	$106.0 \pm 6.7$	$106.0 \pm 6.7$	1.00	0.68	22.38	U
J0943+2805	$42.7 \pm 6.0$	$42.7 \pm 6.0$	1.00	0.75	21.94	U
J0944+3608	$39.1 \pm 7.2$	$113.0 \pm 28.0$	0.35	1.20	22.21	SR
J0946+2056	$77.3 \pm 6.7$	$77.3 \pm 6.7$	1.00	0.70	22.25	U
J0948+4335	$51.6 \pm 7.1$	$124.0 \pm 23.0$	0.42	0.48	22.25	SR
J0950+3926	$154.0 \pm 7.7$	$154.0 \pm 7.7$	1.00	1.00	22.25	U
J0952+2051	$47.8 \pm 2.9$	$47.8 \pm 2.9$	1.00	2.64	22.02	U
J0953+3801	$< 17.1$	$< 17.1$	1.00	0.52	$< 21.57$	ND
J1000+1047	$550.0 \pm 7.7$	$550.0 \pm 7.7$	1.00	2.36	22.89	U

**Table 1.** Continued

Name	$S_p$	$S_{\text{tot}}$	$S_p/S_{\text{tot}}$	$S_A/S_C$	$\log L_{6\text{GHz}}$	Morph.
J1004+1510	$150.0 \pm 9.2$	$243.0 \pm 24.0$	0.62	0.58	22.51	M
J1005+4230	$23.7 \pm 3.4$	$23.7 \pm 3.4$	1.00	0.21	21.65	U
J1007+5007	$31.4 \pm 5.3$	$44.0 \pm 12.0$	0.71	0.44	21.74	SR
J1010+3003	$431.0 \pm 9.1$	$503.0 \pm 18.0$	0.86	1.03	22.97	SR
J1013+0204	$21.9 \pm 2.9$	$21.9 \pm 2.9$	1.00	1.02	21.47	U
J1013+2212	$293.0 \pm 8.3$	$400.0 \pm 23.0$	0.73	1.10	22.94	M
J1021+1900	$35.9 \pm 3.5$	$35.9 \pm 3.5$	1.00	1.20	21.79	U
J1034+6053	$27.6 \pm 7.3$	$143.0 \pm 45.0$	0.19	11.00	22.32	SR
J1036+2750	$31.4 \pm 6.5$	$75.0 \pm 22.0$	0.42	2.56	22.24	SR
J1040+6002	< 13.2	< 13.2	1.00	0.67	<21.54	ND
J1041+2828	$90.3 \pm 5.9$	$118.0 \pm 12.0$	0.77	1.02	22.16	M
J1045+2933	$283.0 \pm 8.0$	$323.0 \pm 15.0$	0.88	1.81	22.91	M
J1045+5202	$132.0 \pm 5.8$	$221.0 \pm 25.0$	0.60	1.13	22.72	M
J1054+3511	$63.2 \pm 6.5$	$83.0 \pm 14.0$	0.76	0.70	21.98	SR
J1100+2838	$22.5 \pm 3.5$	$22.5 \pm 3.5$	1.00	0.74	21.57	U
J1102+0844	$31.6 \pm 5.9$	$31.6 \pm 5.9$	1.00	0.70	22.09	U
J1118+3103	$30.7 \pm 3.2$	$44.9 \pm 7.3$	0.68	0.34	21.98	M
J1120+4235	$40.2 \pm 5.3$	$40.2 \pm 5.3$	1.00	1.36	21.76	U
J1124+4201	$25.9 \pm 4.3$	$25.9 \pm 4.3$	1.00	0.99	21.56	U
J1125+2513	$30.1 \pm 4.7$	$30.1 \pm 4.7$	1.00	0.32	21.81	U
J1129+5120	$104.0 \pm 7.9$	$166.0 \pm 20.0$	0.55	0.66	22.41	SR
J1129+0629	$55.9 \pm 6.5$	$102.0 \pm 18.0$	0.63	0.33	22.22	SR
J1130+0222	$114.0 \pm 5.1$	$114.0 \pm 5.1$	1.00	0.80	22.27	U
J1138+4503	$160.0 \pm 6.2$	$160.0 \pm 11.0$	1.00	1.31	22.63	U
J1146+3715	$43.2 \pm 6.0$	$180.0 \pm 24.0$	0.24	1.98	22.66	M
J1155+5021	$18.3 \pm 7.6$	$204.0 \pm 63.0$	0.09	3.81	22.68	M
J1155+5931	$167.0 \pm 11.0$	$236.0 \pm 24.0$	0.71	0.81	22.59	SR
J1157-0315	$28.5 \pm 0.0$	$28.5 \pm 0.0$	0.34	0.88	21.56	SR
J1157-0022	$47.1 \pm 9.1$	$138.0 \pm 35.0$	1.00	0.05	22.43	SR
J1159+5106	$32.7 \pm 7.5$	$32.7 \pm 7.5$	1.00	0.66	21.93	U
J1202+0225	$29.9 \pm 3.4$	$66.0 \pm 14.0$	0.45	0.15	22.15	M
J1204+1702	$180.0 \pm 8.5$	$215.0 \pm 17.0$	0.84	1.00	22.75	SR
J1206+2814	$35.6 \pm 6.7$	$35.6 \pm 6.7$	1.00	2.57	22.62	U
J1209+0232	$40.7 \pm 8.0$	$93.0 \pm 25.0$	0.44	0.87	22.17	SR
J1210+0154	$42.4 \pm 6.8$	$42.4 \pm 6.8$	1.00	1.19	21.74	U
J1210+2725	$37.7 \pm 6.1$	$72.0 \pm 17.0$	0.52	0.51	22.03	SR
J1212+1859	$68.9 \pm 7.3$	$117.0 \pm 19.0$	0.59	0.68	22.17	SR
J1218+3522	$443.0 \pm 11.0$	$443.0 \pm 11.0$	1.00	0.76	22.86	U
J1220+0641	$319.0 \pm 8.6$	$319.0 \pm 8.6$	1.00	0.81	22.88	U
J1221+2604	$249.0 \pm 8.3$	$293.0 \pm 16.0$	0.85	0.95	22.82	SR
J1233+3101	$22.0 \pm 5.5$	$105.0 \pm 32.0$	0.21	1.70	22.42	E
J1233+6443	$39.0 \pm 5.0$	$203.0 \pm 21.0$	0.19	0.84	22.44	M
J1235+4104	$56.8 \pm 6.2$	$554.0 \pm 67.0$	0.10	2.08	22.84	E

**Table 1.** Continued

Name	$S_p$	$S_{\text{tot}}$	$S_p/S_{\text{tot}}$	$S_A/S_C$	$\log L_{6\text{GHz}}$	Morph.
J1245+0321	$86.0 \pm 6.9$	$137.0 \pm 17.0$	0.63	1.10	22.29	SR
J1248+3424	$50.1 \pm 5.7$	$108.0 \pm 17.0$	0.46	1.17	22.36	SR
J1251+6603	$266.0 \pm 9.9$	$271.0 \pm 18.0$	0.98	1.08	22.80	SR
J1252+1402	$110.0 \pm 7.7$	$110.0 \pm 7.7$	1.00	0.47	22.35	U
J1253+1227	$78.8 \pm 5.4$	$78.8 \pm 5.4$	1.00	0.36	21.97	U
J1302+1406	$55.9 \pm 7.3$	$55.9 \pm 7.3$	1.00	1.27	22.13	U
J1304+0205	$39.6 \pm 5.5$	$227.0 \pm 36.0$	0.17	1.06	22.52	E
J1304+3951	$216.0 \pm 6.6$	$216.0 \pm 6.6$	1.00	0.85	22.66	U
J1307+0107	$74.3 \pm 6.5$	$103.0 \pm 14.0$	0.72	0.75	22.36	SR
J1308+0344	$57.3 \pm 5.4$	$57.3 \pm 5.4$	1.00	1.06	21.95	U
J1308+1904	< 19.8	< 19.8	1.00	0.57	<21.43	ND
J1312+0641	$65.7 \pm 6.2$	$90.0 \pm 14.0$	0.73	0.73	22.17	SR
J1320+2957	$59.9 \pm 9.2$	$123.0 \pm 27.0$	0.49	1.10	22.15	SR
J1321+0459	$55.1 \pm 6.2$	$55.1 \pm 6.2$	1.00	0.34	21.96	U
J1321+3555	< 19.8	< 19.8	1.00	0.24	<21.67	ND
J1322+3623	$77.1 \pm 7.4$	$195.0 \pm 25.0$	0.40	1.27	22.70	SR
J1330+3119	$153.0 \pm 6.8$	$153.0 \pm 6.8$	1.00	1.41	22.40	U
J1334+1711	$32.3 \pm 6.8$	$32.3 \pm 6.8$	1.00	0.31	21.82	U
J1348+4518	$50.7 \pm 4.3$	$50.7 \pm 4.3$	1.00	0.70	22.05	U
J1348+4303	$62.4 \pm 6.3$	$62.4 \pm 6.3$	1.00	0.98	22.14	U
J1353+3620	$449.0 \pm 11.0$	$449.0 \pm 11.0$	1.00	1.41	23.12	U
J1406+1442	$116.0 \pm 6.6$	$116.0 \pm 6.6$	1.00	0.80	22.37	U
J1408+4303	$27.5 \pm 5.6$	$75.0 \pm 21.0$	0.37	0.14	22.16	E
J1408+6306	< 23.1	< 23.1	1.00	0.59	<21.65	ND
J1412+6435	$50.6 \pm 8.2$	$50.6 \pm 8.2$	1.00	1.51	22.09	U
J1421+1520	$66.7 \pm 8.0$	$106.0 \pm 19.0$	1.00	0.66	22.20	SR
J1421+0739	$67.0 \pm 5.5$	$67.0 \pm 5.5$	1.00	0.59	22.00	U
J1425+0803	$194.0 \pm 7.9$	$220.0 \pm 15.0$	0.88	1.59	22.51	SR
J1426+1955	$30.9 \pm 5.7$	$30.9 \pm 5.7$	1.00	0.28	21.59	U
J1429+4747	$88.6 \pm 8.5$	$151.0 \pm 21.0$	0.59	1.19	22.31	M
J1442+4337	$183.0 \pm 7.4$	$183.0 \pm 7.4$	1.00	1.10	22.44	U
J1443+4045	$78.0 \pm 11.2$	$78.0 \pm 11.2$	1.00	0.27	21.56	U
J1444+0633	$256.0 \pm 7.2$	$361.0 \pm 23.0$	0.71	1.42	22.63	E
J1445+3049	$60.1 \pm 7.0$	$60.1 \pm 7.0$	1.00	0.91	22.12	U
J1456+2750	$136.0 \pm 7.0$	$136.0 \pm 7.0$	1.00	0.86	22.38	U
J1458+4555	$33.0 \pm 4.8$	$33.0 \pm 4.8$	1.00	1.24	21.90	U
J1458+3631	$50.6 \pm 6.1$	$207.0 \pm 31.0$	1.00	0.35	22.55	SR
J1502+0645	$17.8 \pm 4.2$	$17.8 \pm 4.2$	1.00	0.35	21.64	U
J1521+5940	$22.5 \pm 5.5$	$108.0 \pm 32.0$	0.21	2.52	22.41	SR
J1524+3032	$29.7 \pm 3.8$	$29.7 \pm 3.8$	1.00	0.47	21.81	U
J1526+2754	$28.3 \pm 5.3$	$28.3 \pm 5.3$	1.00	0.93	21.63	U
J1527+1541	$42.7 \pm 6.7$	$60.0 \pm 15.0$	0.71	0.82	21.94	SR
J1529+0216	$41.2 \pm 6.4$	$183.0 \pm 34.0$	0.23	1.20	22.56	E

**Table 1.** Continued

Name	$S_p$	$S_{\text{tot}}$	$S_p/S_{\text{tot}}$	$S_A/S_C$	$\log L_{6\text{GHz}}$	Morph.
J1534+4658	$18.7 \pm 3.9$	$18.7 \pm 3.9$	1.00	0.28	21.64	U
J1535+5644	$124.0 \pm 7.7$	$124.0 \pm 7.7$	1.00	0.98	22.16	U
J1539+5042	$51.4 \pm 5.5$	$51.4 \pm 5.5$	1.00	0.83	21.76	U
J1544+2827	$21.7 \pm 4.8$	$21.7 \pm 4.8$	1.00	0.47	21.51	U
J1556+5215	$274.0 \pm 6.3$	$274.0 \pm 6.3$	1.00	0.93	22.59	U
J1605+4834	$25.9 \pm 7.6$	$25.9 \pm 7.6$	1.00	0.32	21.82	U
J1617+0638	$466.0 \pm 7.1$	$466.0 \pm 7.1$	1.00	1.75	22.83	U
J1617+0854	$300.0 \pm 8.2$	$387.0 \pm 18.0$	0.78	1.01	22.65	SR
J1619+5011	$30.8 \pm 4.5$	$30.8 \pm 4.5$	1.00	0.86	21.67	U
J1619+2543	$345.0 \pm 9.5$	$407.0 \pm 22.0$	1.00	0.74	22.93	SR
J1627+4736	$441.0 \pm 12.0$	$441.0 \pm 12.0$	1.00	1.47	22.94	U
J1630+4711	$33.9 \pm 5.6$	$33.9 \pm 5.6$	1.00	0.53	21.85	U
J1631+4048	$26.6 \pm 4.6$	$26.6 \pm 4.6$	1.00	0.54	21.70	U
J1631+2953	$67.6 \pm 5.7$	$67.6 \pm 5.7$	1.00	0.54	22.10	U
J1703+1910	$< 11.4$	$< 11.4$	1.00	0.54	$< 21.45$	ND
J1727+6322	$53.6 \pm 6.1$	$670.0 \pm 82.0$	0.08	0.92	22.94	E

## B. OPTICAL DATA

Data in Table 2 is listed as follows:

- **Column 1:** Full name of the QSO in SDSSJ format
- **Column 2:** Redshift from the SDSS-DR7 catalog (Schneider et al. 2010)
- **Column 3:** Angular offset of the QSO's detected radio component to its optical position; typical uncertainties in the optical positions of SDSS quasars are  $\approx 0.1''$
- **Column 4:** Absolute  $i$ -band magnitude
- **Column 5:** Apparent  $i$ -band magnitude
- **Column 6:** Base-10 logarithm of  $R$ , the ratio between our measured total 6 GHz flux density at  $0.33''$  and the targets' corresponding optical flux density in the  $i$ -band

**Table 2.** Target Quasar Optical Properties

(1)	(2)	(3)	(4)	(5)	(6)
Name (SDSSJ)	$z$	$\Delta$ ( $''$ )	$M_i$	$m_i$	$\log R$
080829.17+440754.1	0.275	0.15	-22.58	17.615	-0.95
081652.24+425829.4	0.234	0.15	-23.21	16.636	-0.61
082205.24+455349.1	0.300	0.07	-22.69	17.695	0.24
083443.80+382632.8	0.288	0.08	-22.77	17.527	-0.48
084313.41+535718.8	0.218	0.15	-23.25	16.440	-0.44
084755.63+263147.6	0.282	0.10	-22.59	17.662	-0.88
085828.69+342343.8	0.257	0.22	-23.89	16.156	-0.82

**Table 2.** Continued

Name	$z$	$\Delta$	$M_i$	$m_i$	$\log R$
090454.99+511444.5	0.225	6.20	-23.12	16.637	-1.31
090725.91+021521.1	0.273	0.14	-23.09	17.091	-1.42
092309.87+453046.4	0.292	0.04	-22.58	17.747	-0.71
092909.79+464424.0	0.240	0.05	-23.82	16.085	-1.24
093433.95+030645.1	0.297	0.00	-22.68	17.681	-0.99
093509.48+481910.2	0.224	0.04	-22.73	17.026	-0.03
094254.05+345133.1	0.278	0.10	-22.63	17.594	-0.50
094305.15+280536.1	0.267	0.03	-22.68	17.457	-0.95
094427.99+360837.1	0.228	0.09	-22.76	17.030	-0.69
094636.42+205610.9	0.280	0.09	-22.91	17.321	-0.74
094859.47+433518.9	0.226	0.12	-23.40	16.367	-0.92
095048.38+392650.4	0.206	0.10	-23.62	15.952	-0.99
095236.13+205143.5	0.276	0.14	-22.59	17.615	-0.83
095302.64+380145.2	0.273	0.00	-22.69	17.493	-1.33
100033.88+104723.7	0.226	0.13	-23.53	16.244	-0.32
100438.82+151057.3	0.219	0.09	-22.86	16.841	-0.44
100528.34+423037.5	0.257	0.09	-23.31	16.736	-1.49
100744.54+500746.6	0.212	0.28	-22.83	16.800	-1.20
101000.68+300321.5	0.256	0.13	-23.11	16.930	-0.09
101312.15+020416.4	0.220	0.04	-22.92	16.792	-1.50
101325.43+221229.4	0.274	0.05	-22.71	17.474	0.03
102101.20+190012.3	0.247	0.15	-23.14	16.820	-1.28
103421.71+605318.1	0.228	0.09	-22.67	17.118	-0.56
103609.28+275019.9	0.282	0.04	-22.82	17.436	-0.71
104041.50+600239.3	0.297	0.00	-22.59	17.771	-1.33
104111.97+282805.0	0.211	0.15	-23.45	16.170	-1.02
104528.30+293344.7	0.293	0.11	-22.75	17.581	-0.02
104541.76+520235.5	0.284	0.04	-23.51	16.760	-0.51
105416.19+351124.1	0.205	0.09	-22.78	16.783	-0.93
110052.34+283801.2	0.243	0.08	-22.81	17.119	-1.36
110205.92+084435.7	0.294	0.99	-24.00	16.344	-1.34
111842.83+310317.4	0.270	0.02	-22.71	17.444	-0.93
112007.43+423551.3	0.227	0.10	-22.93	16.848	-1.22
112439.18+420145.0	0.225	0.08	-24.14	15.623	-1.90
112503.68+251302.3	0.272	0.18	-22.98	17.191	-1.21
112959.40+062952.9	0.241	0.08	-22.67	17.245	-0.65
112941.94+512050.5	0.234	0.13	-22.83	17.019	-0.53
113020.99+022211.5	0.241	0.15	-22.63	17.285	-0.59
113858.79+450338.5	0.300	0.05	-22.91	17.475	-0.37
114646.02+371511.7	0.295	4.09	-23.32	17.032	-0.49
115549.43+502117.2	0.284	0.09	-22.81	17.456	-0.27
115558.97+593129.2	0.241	0.11	-22.63	17.278	-0.28
115758.72-002220.9	0.260	0.16	-22.84	17.230	-0.53

**Table 2.** Continued

Name	$z$	$\Delta$	$M_i$	$m_i$	$\log R$
115753.20-031537.1	0.215	0.00	-22.86	16.801	-1.38
115901.72+510630.7	0.296	0.15	-22.82	17.532	-1.03
120233.08+022559.7	0.273	0.06	-22.89	17.292	-0.82
120447.91+170256.8	0.298	0.09	-23.29	17.084	-0.39
120629.36+281436.1	0.293	0.81	-22.90	17.433	-0.37
120944.81+023212.7	0.238	0.07	-22.61	17.276	-0.68
121018.34+015405.9	0.216	0.18	-22.76	16.914	-1.17
121045.63+272536.4	0.230	0.07	-22.83	16.979	-0.91
121224.89+185920.1	0.215	0.15	-22.69	16.972	-0.70
121832.68+352255.8	0.240	0.07	-22.64	17.266	-0.01
122018.43+064119.6	0.286	0.17	-22.83	17.455	-0.07
122157.77+260457.7	0.278	0.06	-22.97	17.249	-0.19
123341.68+310102.8	0.291	0.16	-23.55	16.771	-0.83
123341.80+644317.4	0.222	3.17	-22.63	17.105	-0.41
123532.83+410445.1	0.212	0.10	-22.82	16.811	-0.09
124551.03+032128.3	0.227	0.18	-22.81	16.966	-0.64
124853.89+342429.4	0.271	0.18	-22.61	17.552	-0.51
125100.44+660326.8	0.282	0.07	-23.49	16.764	-0.42
125236.15+140213.9	0.266	0.16	-22.67	17.453	-0.54
125343.71+122721.5	0.207	0.21	-22.71	16.874	-0.91
130223.12+140609.0	0.286	0.04	-23.42	16.859	-1.07
130416.99+020537.0	0.229	0.19	-22.75	17.046	-0.39
130456.91+395111.4	0.271	0.04	-22.66	17.504	-0.22
130756.57+010709.6	0.276	0.12	-23.17	17.033	-0.73
130818.89+034437.2	0.228	0.11	-23.19	16.599	-1.14
130843.86+190439.7	0.222	0.00	-22.98	16.756	-1.56
131204.70+064107.5	0.242	0.17	-24.02	15.901	-1.25
132059.41+295728.1	0.206	0.20	-22.65	16.918	-0.70
132123.40+045930.7	0.242	0.16	-22.95	16.970	-1.03
132136.86+355553.4	0.283	0.00	-23.24	17.018	-1.46
132257.89+362300.0	0.295	1.61	-22.70	17.650	-0.21
133053.27+311930.5	0.242	0.13	-22.75	17.170	-0.51
133432.34+171146.9	0.265	0.20	-23.17	16.951	-1.27
134854.76+430309.1	0.275	0.17	-23.11	17.090	-0.93
134845.44+451809.5	0.277	0.16	-23.00	17.208	-0.97
135326.12+362049.4	0.285	0.14	-24.26	16.011	-0.42
140658.70+144238.3	0.266	0.13	-23.50	16.629	-0.84
140808.19+430316.5	0.258	0.05	-23.14	16.922	-0.92
140839.00+630600.5	0.261	0.00	-23.13	16.950	-1.42
141213.62+643538.9	0.288	0.16	-22.84	17.459	-0.87
142146.16+073908.3	0.231	0.07	-22.93	16.887	-0.98
142138.50+152045.9	0.231	0.11	-22.65	17.164	-0.67
142522.37+080327.1	0.230	0.21	-23.01	16.803	-0.50

**Table 2.** Continued

Name	$z$	$\Delta$	$M_i$	$m_i$	$\log R$
142613.31+195524.6	0.213	0.20	-23.34	16.300	-1.60
142943.07+474726.2	0.221	0.00	-23.23	16.490	-0.79
144202.82+433708.7	0.231	0.12	-22.97	16.849	-0.56
144302.59+404525.1	0.246	0.00	-23.32	16.636	-1.58
144414.66+063306.7	0.208	0.09	-23.04	16.552	-0.38
144510.13+304957.0	0.276	0.19	-22.74	17.466	-0.79
145608.65+275008.7	0.248	0.05	-22.93	17.044	-0.61
145824.46+363119.5	0.246	0.23	-23.07	16.887	-0.49
145817.42+455514.9	0.286	0.07	-22.90	17.381	-1.09
150204.10+064516.0	0.288	0.15	-23.52	16.772	-1.60
152153.80+594020.0	0.286	0.38	-22.60	17.679	-0.45
152428.67+303237.5	0.274	0.07	-23.57	16.618	-1.44
152624.02+275452.1	0.231	0.19	-23.61	16.213	-1.62
152727.38+154100.1	0.228	0.11	-23.18	16.607	-1.14
152925.98+021646.6	0.263	0.03	-22.61	17.490	-0.30
153415.05+465819.2	0.282	0.12	-22.75	17.500	-1.30
153539.25+564406.5	0.207	0.05	-22.91	16.672	-0.80
153941.49+504255.7	0.203	0.05	-22.81	16.725	-1.16
154430.52+282756.8	0.231	0.18	-23.53	16.285	-1.71
155620.23+521520.0	0.227	0.23	-22.91	16.870	-0.37
160507.92+483422.1	0.295	0.11	-23.57	16.775	-1.44
161711.42+063833.4	0.229	0.08	-23.17	16.627	-0.24
161723.67+085414.7	0.206	0.04	-23.31	16.255	-0.47
161940.56+254323.0	0.269	0.14	-23.50	16.644	-0.29
161911.24+501109.2	0.234	0.16	-22.86	16.991	-1.28
162750.54+473623.5	0.262	0.16	-22.87	17.218	-0.03
163051.74+471118.9	0.270	0.08	-23.25	16.910	-1.27
163124.42+295301.5	0.254	0.18	-23.32	16.707	-1.05
163111.28+404805.2	0.258	0.08	-22.96	17.094	-1.30
170302.88+191034.0	0.290	0.00	-23.11	17.203	-1.62
172711.80+632242.1	0.217	0.29	-22.95	16.730	-0.04